CHINESE OPTICS LETTERS
Vol. 19, No. 4 | April 2021

Floquet spectrum and optical behaviors in dynamic Su–Schrieffer–Heeger modeled waveguide array

Ye Yu (余 晔)[1], Yiwen Song (宋一雯)[1], Tao Chen (陈 焘)[1], Huaiqiang Wang (王怀强)[2*], Songlin Zhuang (庄松林)[1], and Qingqing Cheng (程庆庆)[1**]

[1] School of Optical-Electrical and Computer Engineering, University of Shanghai for Science and Technology, Shanghai 200093, China

[2] National Laboratory of Solid State Microstructures, School of Physics, Nanjing University, Nanjing 210093, China

*Corresponding author: hqwang@nju.edu.cn

**Corresponding author: qqcheng@usst.edu.cn

Received July 3, 2020 | Accepted October 9, 2020 | Posted Online January 4, 2021

Floquet topological insulators (FTIs) have been used to study the topological features of a dynamic quantum system within the band structure. However, it is difficult to directly observe the dynamic modulation of band structures in FTIs. Here, we implement the dynamic Su–Schrieffer–Heeger model in periodically curved waveguides to explore new behaviors in FTIs using light field evolutions. Changing the driving frequency produces near-field evolutions of light in the high-frequency curved waveguide array that are equivalent to the behaviors in straight arrays. Furthermore, at modest driving frequencies, the field evolutions in the system show boundary propagation, which are related to topological edge modes. Finally, we believe curved waveguides enable profound possibilities for the further development of Floquet engineering in periodically driven systems, which ranges from condensed matter physics to photonics.

Keywords: topological photonics insulator; waveguide array; Floquet.

DOI: 10.3788/COL202119.042601

1. Introduction

Recently, photonic topological insulators have been cutting-edge research topics in condensed matter physics because of the emergence of topologically protected states located at interfaces[1,2]. Interface states in static topological systems are characterized by their immunity to perturbations, which have given rise to many interesting phenomena and potential applications[1–6]. The topological characteristics in the dynamics of driven quantum systems provide newly engineered, topologically nontrivial phases that are not accessible in static systems[7]. Therefore, a series of early works developed the notion of a "Floquet topological insulator" (FTI)[8], which can appropriately modulate the drive frequency[7], amplitude[3], and symmetry to engineer the topological features of a band structure[9,10]. Over the past decade, FTI has been explored in many systems, such as cold atoms[11,12], photonics[13,14], and solid-state systems[15–17]. However, directly observing these effects in the above systems is difficult. Consequently, the lack of equivalent visualized systems has greatly hindered further developments of Floquet band engineering.

To date, many classical systems have been developed to imitate these behaviors in quantum systems, such as cold atoms[18], photonic crystal[19], metamaterials[20,21], and waveguide arrays[22–26]. In particular, the propagation constant and coupling strength of waveguides can be flexibly controlled through periodic curving and changes in its shape, which allows studying the dynamics of driven quantum effects. Furthermore, curved waveguides have many equivalent physical mechanisms. It is noted that Bloch oscillation[27,28], dynamic localization[29–31], and the evolution of massless Dirac particles can be demonstrated in curved waveguides[32–34]. These works showed that curved waveguides could introduce new physics into photonics simulators relative to straight waveguides. Curved waveguide arrays, as first described in Ref. [13], have been used to study FTI in the adiabatic range, where temporal variations in solid-state systems induce topological edge states. Many works have investigated the behaviors of Floquet systems by detecting the electromagnetic fields in curved arrays, where the appearance of localized modes is related to the Floquet band structure of the system[35–38]. For example, our recent work applied Floquet theory to describe the one-dimensional (1D) dynamic Su–Schrieffer–Heeger (SSH) model for a periodically curved waveguide array in the non-adiabatic range and observed the anomalous Floquet π mode in a microwave periodic curved coplanar waveguide array[39]. However, the relationship between optical behaviors and the Floquet band structure has been unclear in periodically curved waveguides as dictated by the driving frequency[39,40].

This paper shows the design for a silicon waveguide array with a slow to fast curving profile, which corresponds to a periodically driven frequency from an adiabatic approach to the high-frequency range. The simulated results for the 1D dynamic SSH model of a periodically curved waveguide array illustrate the behavior of the energy transfer on these two boundary waveguides. At high frequencies, the results suggest that a curved waveguide is equivalent to a straight waveguide. In addition, localized light propagates along the array boundary, which exhibits steady-state behaviors in a periodically driven system at modest frequencies. At low frequencies, the light propagation behaves chaotically in the arrays.

2. Theory of Periodically Driven SSH Model

We consider a variant of the dynamic SSH model to search for Floquet topological phases. The SSH model has two bands and describes spinless fermions that hop on a 1D tight-binding lattice with staggered amplitudes. Figure 1 is a schematic illustration of the SSH model for a periodically curved waveguide array. The array consists of silicon waveguides with widths W of 500 nm and heights H of 220 nm and guides a single-mode excited by infrared light at 1550 nm. Along the propagating direction z of the array, the nearest-neighboring (NN) waveguides are coupled with opposite axis offsets and spacings of $G(z) = G \pm 2A_0 \cos(2\pi z/\Lambda)$, as shown in Fig. 1, where $G = 360$ nm and $A_0 = 50$ nm are the initial spacing without bending and the amplitude, respectively. The co-sinusoidal bending of the NN waveguides is in the opposite direction, where Λ is the period of the cosine-modulated structures. Coupled-mode theory allows for mapping the waveguide array into an effective 1D time-dependent tight-binding-approximated Hamiltonian as

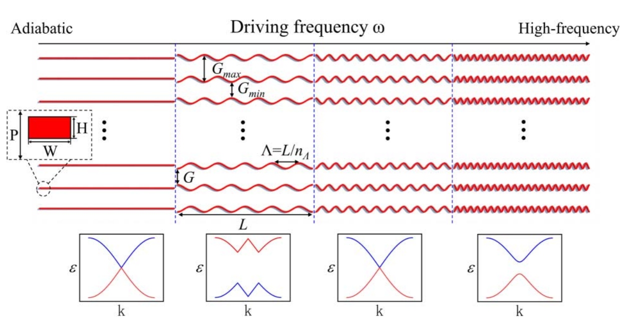

Fig. 1. Schematic illustration of a periodically bent silicon waveguide array with a cosine modulation of the spacing G between adjacent waveguides in the propagation direction z to illustrate the band structure of the waveguide array at different frequencies. The inset magnifies the rectangular waveguide structure with parameters $P = 5\,\mu\text{m}$, $H = 220$ nm, and $W = 500$ nm.

$$H_S = \sum_{n=1}^{N}(\kappa_0 - \delta\kappa)c^{\dagger}_{A,n}c_{B,n} + \sum_{n=1}^{N-1}(\kappa_0 + \delta\kappa)c^{\dagger}_{B,n}c_{A,n} + \text{h.c.}, \quad (1)$$

where $c^{\dagger}_{A(B),n}$ and $c_{A(B),n}$ are the creation and annihilation operators of electrons on sublattices A and B, respectively, and $\kappa_0 - \delta\kappa$ and $\kappa_0 + \delta\kappa$ represent the staggered hopping strengths of the intercell and intracell coupling, respectively. The energy gap in the SSH model is closed when $\delta\kappa$ is equal to zero. We express the usual coupled-mode equation with the real-space Hamiltonian form as $\hat{H}\varphi(z) = E_{2N}\varphi(z)$, here

$$\hat{H}(z) = \begin{bmatrix} \beta & \kappa_1(z) & & & & \\ \kappa_1(z) & \beta & \kappa_2(z) & & & \\ & \kappa_2(z) & \ddots & \ddots & & \\ & & \ddots & \ddots & \kappa_2(z) & \\ & & & \kappa_2(z) & \beta & \kappa_1(z) \\ & & & & \kappa_1(z) & \beta \end{bmatrix}_{N\times N}, \quad (2)$$

where N is the total number of waveguides, and β is the effective propagation constant in a single-mode waveguide. The NN couplings gradually increase based on the $\kappa_1(z) = \kappa_0 - \Delta\kappa$ to $\kappa_2(z) = \kappa_0 + \Delta\kappa$ from Eq. (2) and shown in Fig. 1, where κ_0 is the average coupling coefficient without bending, and $\Delta\kappa$ is the staggered coupling coefficient. In our design, the NN coupling coefficient κ describes the relationship between the distance $G(z)$ and the coupling strength, which can be approximated as $\kappa_0 \pm \delta\kappa_0 \cos(2\pi z/\Lambda)$, where $\kappa_0 = 0.015\,\mu\text{m}^{-1}$ and $\delta\kappa_0 = 0.01\,\mu\text{m}^{-1}$. Compared with the Hamiltonian in Eq. (2), we transform the static SSH model into its dynamic variant to study a curved waveguide array by modulating $\delta\kappa$ along the propagation direction z. We steer the dynamic SSH waveguide with periodic curving to link the system with an FTI. The principles of FTIs indicate that the energy gap of the arrays changes along the propagation z, which switches based on the modulated parameter $\Delta\kappa$. However, the instantaneous $H(z)$ cannot describe the topological characteristics of the time-dependent energy gap in the arrays. Instead, we use the effective Floquet Hamiltonian H_F to represent the arrays, which is the time average of $H(z)$ over a period Λ. As shown in the center part of Fig. 1, the energy gap is closed for uniform straight waveguide arrays. We then change the driving frequency of the arrays from adiabatic to high frequency, and the energy gap undergoes opening, closing, and reopening, as shown in the bottom of Fig. 1. At modest frequencies, the light propagation shows steady-state behaviors in the array, and the energy gap is open, as shown in Fig. 1. Thus, the propagation behavior of light at high frequencies is approximately equal to a straight channel.

We use Floquet's theorem to understand the physical mechanism of the localized propagation behavior induced by periodically engineered waveguide arrays. Thus, Schrödinger's equation is

$$i\hbar \frac{\partial}{\partial z}\psi(z) = H(z)\psi(z), \tag{3}$$

where the time-periodic Hamiltonian $H(z) = H(z + \Lambda)$ governs the time evolution of the driven system. We define $\omega = 2\pi/\Lambda$ as the driving frequency, as shown in Fig. 1. The complete set of orthogonal solutions to Eq. (3) is $\psi(z) = \exp(-i\varepsilon z/\hbar)\phi(z)$ with $\phi(z) = \phi(z + \Lambda)$. Here, the "quasi-energy" ε plays a role analogous to the energy of a Hamiltonian eigenstate in a non-driven system. The quasi-energy spectrum is determined by the Floquet operator $U(z,z_0) = \Gamma \exp[-(i/\hbar)\int_{z_0}^{z} \mathrm{d}z H(z)]$, where Γ denotes the time-ordering operator for a one-period evolution, and z_0 is the initial time. To simplify the notation, we set $z_0 = 0$ and $U(z,z_0) = U(z)$. The Floquet operator is defined as the time evolution for one full period and is given by $U(\Lambda)$, from which the time-averaged effective Hamiltonian is derived as $H_F = (i/\Lambda)\ln|U(\Lambda)|$. Figure 2(a) plots the quasi-energy spectrum with changes in the driving frequency ω by numerically solving H_F.

It is noted that the band structure of the system describes light propagation in the arrays with representative points of $\omega/\Delta = 0$, $\omega/\Delta = 1.6$, and $\omega/\Delta = 1/3$. The spectrum remains unchanged in the high-frequency range ($\omega/\Delta = 1.6$) when changing the driving frequency, which is equivalent to the undriven case at the point $\omega/\Delta = 0$ at lower frequencies. The quasi-energy gap undergoes closing and re-opening processes at $\omega/\Delta = 1$ and $\omega/\Delta = 1/3$, respectively. Of note, the anomalous dynamic end modes emerge in the waveguide array at these frequencies, which was previously proven to be the Floquet π mode[39].

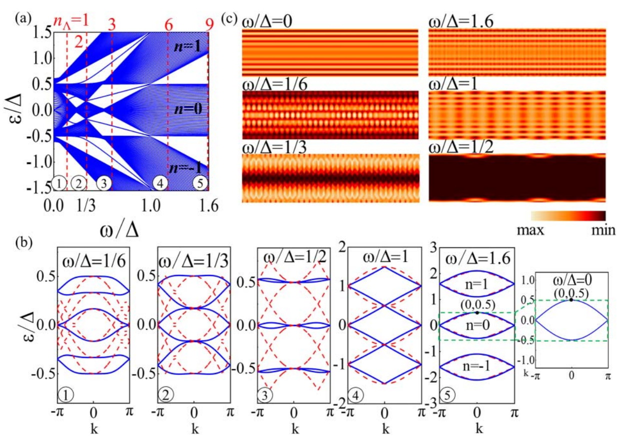

Fig. 2. (a) Quasi-energies under open-boundary conditions with 40 waveguides where the bandwidth Δ is taken as the energy unit. (b) The momentum space quasi-energy band structure (blue solid lines) of the five chosen frequency replicas and the straight cases with $\omega/\Delta = 1/6$, $\omega/\Delta = 1/3$, $\omega/\Delta = 1/2$, $\omega/\Delta = 1$, $\omega/\Delta = 1.6$, and $\omega/\Delta = 0$. Red dashed lines correspond to the case with no dimerization ($\delta\kappa = 0$) and uncoupled Floquet replicas to guide the eye for each Floquet replica. (c) The dynamic evolution of the array system for the 20 waveguides with the six frequencies shown in (b).

Furthermore, we choose the five modulated frequency points to plot their energy band diagram in momentum space as well as the dynamic evolution of the system, which is shown in Figs. 2(b) and 2(c).

We first consider the high-frequency case by choosing the representative point at $\omega/\Delta = 1.6$. The driving frequency is larger than the undriven system bandwidth ($\Delta = 4\kappa_0$). The drive cannot resonantly couple the states in the $n = \pm 1$ and $n = 0$ bands for any value of k in the Brillouin zone [see Fig. 2(b)]. Here, the essential effect of the drive is to lift the degeneracy at the band crossing point where the $n = 0$ and $n = \pm 1$ bands touch. In this regime, the system is governed primarily by the low-energy Hamiltonian ($n = 0$ band). To explain this phenomenon, we use two techniques to compute the effective Floquet Hamiltonian at high frequencies (see Appendix A for a full derivation). In both cases, we decompose the Floquet Hamiltonian $H_{F[z_0]}$ as

$$H_{F[z_0]} \approx {}^{(0)}H + \frac{2i \sin \omega z_0}{\omega}[{}^{(1)}H, {}^{(0)}H], \tag{4}$$

where z_0 is the initial position of the propagation direction (time axis), and H_0 and $H_{\pm 1}$ are the Fourier components of the time-periodic Hamiltonian of Eq. (1) shown as

$$H(z) = \sum_{l=0}^{\infty} {}^{(l)}H_l e^{il\omega z}. \tag{5}$$

Here, the second term of the effective Floquet Hamiltonian in Eq. (4) becomes approximately zero, which is in the fast-driving regime ($\omega \to \infty$). In this state, $H_{F[z_0]}$ reduces to H_0, which is the same as a straight waveguide. This indicates that periodically driven arrays at high frequencies can be equal to a straight array for light propagation. To further support this argument, we compare the dynamic evolution between the high-frequency $\omega/\Delta = 1.6$ and the undriven state $\omega/\Delta = 0$, as shown in Fig. 2(c). The majority of the energy distributions are the same in both cases.

The modest frequency of $\omega/\Delta = 1/3$ between the $n = 0$ and $n = \pm 1$ bands is the region where the isolated bound quasi-stationary modes are formed in the gap area of the spectrum. The optical boundary mode exhibits steady-state behaviors in the boundary arrays when the $n = 0$ and $n = \pm 1$ bands open at the band crossing points, which is topologically nontrivial. Floquet boundary modes (FBMs) propagate along the array boundaries as a dynamic evolution within the modest frequency range ($1/3 < \omega/\Delta < 1$), where the energy gap is typically open. It is noted that the FBMs are stronger when the energy gap increases compared with the results at the $\omega/\Delta = 1/3$ and $\omega/\Delta = 1/2$ frequencies, as shown in Fig. 2(c).

3. Simulation Results

Eight waveguides are coupled into an array with a propagation distance of $L = 600\,\mu\mathrm{m}$ in the simulations. The driving frequency is given by $\omega = 2\pi/\Lambda = 2\pi n_\Lambda/L$, as shown in Fig. 1, where n_Λ is the total number of periods contained in L. For a fixed L, n_Λ is adjusted to investigate the various frequency-dependent non-static phenomena in the driven waveguide array. We begin at the high-frequency regime where the period Λ is much smaller than the effective coupling length. In this case, light propagation in a periodically driven waveguide array is similar to a straight array as they are unaffected by the fast-period bending. We use the finite-difference time-domain (FDTD) method to perform simulations of the amplitude E_z profile after injecting a light wave at 1550 nm from the upmost boundary of the array, which is shown in Fig. 3(a). As expected, the light propagation behavior resembles that of the straight waveguides with an identical NN coupling. The light spreads from the upmost boundary to the bottom, which is the topologically trivial state for the two cases.

As a comparison between the high-frequency and straight case, we plot the field for each array for the two different states, as shown in Fig. 3(b). The light propagates along the same direction in the two systems, which is represented by the peaks of the field amplitude and illustrated as the black and green lines in Fig. 3(b). Minor differences between the local details of the propagation patterns for the two cases may stem from the bending structure in the fast-varying profile. It is noted that the high driving frequency has a negligible effect, which contrasts with the case of dynamic localization obtained for high-frequency driven quantum-mechanical lattice models with electromagnetic fields. To prove that the principle is still useful for observing topological edge states in the dynamic SSH model, we design the $N = 4$ and $n_\Lambda = 9$ periodically driven waveguides array, where the boundary NN coupling is smaller than the central NN coupling. This simulates the adiabatic elimination effect in periodically driven arrays,[41,42] where light propagates primarily between the first and fourth waveguides, as shown in Fig. 3(c). The equivalent behavior in the high-frequency regime indicates a straight waveguide array with the corresponding NN coupling, as shown in Fig. 3(d). This suggests that the high-frequency approximation can be used in the quantum simulations of adiabatic systems.

We gradually decreased the driving frequency to the range of $n_\Lambda = 1$–6, as shown in Fig. 4. Figure 4(a) shows that the light propagates from the injected upmost waveguide to the bottom, which is topologically trivial and like the state in Fig. 3(a). Comparing Fig. 3(a) with Fig. 4(a) shows that the light propagation behavior becomes dissimilar with the straight system, which is represented by the propagation length along z, as the driving frequency decreases from $n_\Lambda = 9$ to $n_\Lambda = 6$. This demonstrates that the energy gap between $n = 0$ and $n = \pm 1$ becomes close as the driving frequency is close to the undriven system bandwidth ($\omega \to \Delta$), which is shown in Fig. 2(b). As the frequency decreases from $n_\Lambda = 6$ to $n_\Lambda = 4$, light propagation in the arrays tends to localize in the upmost boundary where the system starts to become topologically nontrivial. At the modest frequency of $n_\Lambda = 3$, a distinct propagation field pattern arises along the array boundary, as shown by the simulation results in Fig. 4(b). The injected light wave no longer spreads into the bulk array but is instead localized primarily within the two waveguides at the upper boundary. The localized field profile exhibits a periodic oscillation pattern in its distribution between the boundary waveguides, as shown in Fig. 4(c). An anomalous edge mode was observed in an ultrathin metallic array of coupled corrugated waveguides, which is shown to be the long pursued Floquet π mode in the Floquet SSH model[39]. As the driving frequency decreases to $n_\Lambda = 1$ in Fig. 4(d), the

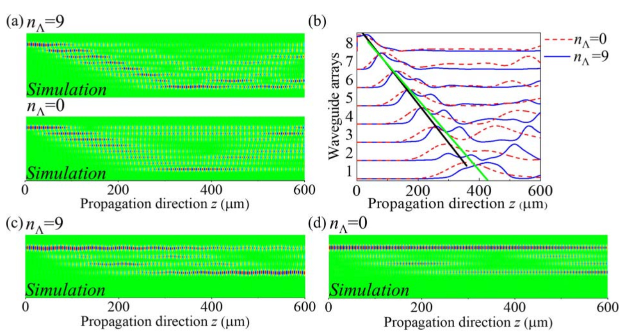

Fig. 3. FDTD simulations of E_z evolution patterns after injecting light from the upmost boundary waveguide under different driving conditions with the same length of $L = 600\,\mu m$. (a) The results for the curved ($n_\Lambda = 9$) and straight ($n_\Lambda = 0$) waveguide arrays with waveguide number $N = 8$. (b) The blue solid and red dashed lines correspond to the propagation of each array, where the black and green lines represent the light propagation direction with the driving frequency ($n_\Lambda = 9$ and $n_\Lambda = 0$). (c) FDTD simulation of the amplitude profiles for the $N = 4$ waveguide array with $n_\Lambda = 9$, $G_{max} = 460\,\mu m$, and $G_{min} = 260\,\mu m$. (d) The results for the straight $N = 4$ waveguide array with the adiabatic elimination effect.

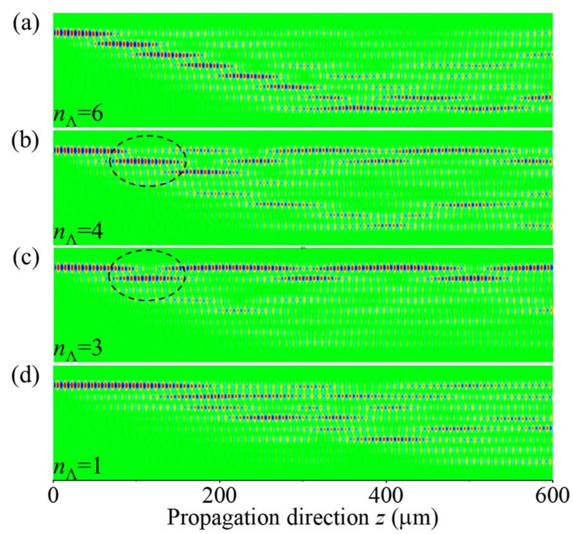

Fig. 4. FDTD simulations of E_z evolution patterns when injecting light from the upmost boundary waveguide, with different driving periodic numbers at the same length of $L = 600\,\mu m$ in simulation. The black dashed circles in (b) and (c) show that the localized field profile exhibits a periodic oscillation pattern between the two boundary waveguides.

light propagation spreads from the injected upper layer to the bulk array without stroboscopic evolution, which is within the topologically trivial phase.

4. Conclusion

In summary, we realized a photonic simulator for the Floquet engineering of quasi-energy bands in 1D dynamic SSH models for a finite, periodic, and curved silicon waveguide array. We observe the high-frequency approximation effects for a given frequency along with the dynamic localized end modes in the 1D periodically driven system. We illustrate that the high-frequency driven Floquet Hamiltonian in the dimerized-driven SSH model for a finite waveguide array is equivalent to the static Hamiltonian in a straight waveguide array. We also observe that light boundary propagation is dictated by the Floquet π modes in the curved waveguides at the modest frequency regime. At the low-frequency regime, the light behavior tends to be disordered in the waveguide arrays. The visualized engineering of the Floquet simulator allows designing "on-demand" architectures with the required band structure.

Appendix A

To compute the Floquet effective Hamiltonian, we provide the effective Hamiltonian and the kick operator as

$$H_F = \sum_{n=0}^{\infty} H_F^{(n)}, \quad K_F = \sum_{n=0}^{\infty} K_F^{(n)}. \tag{A1}$$

Using the formal Baker-Campbell-Hausdorff formula, one finds the perturbative given by

$$H_F^{(0)} = {}^{(0)}H = \frac{1}{\Lambda}\int_0^{\Lambda} \mathrm{d}z H(z), \tag{A2}$$

$$H_F^{(1)} = \frac{1}{\Lambda}\sum_{n=1}^{\infty}\frac{1}{n}[{}^{(n)}H,\ {}^{(-n)}H] = \frac{1}{\Lambda}[{}^{(n)}H,\ {}^{(-n)}H] = 0, \tag{A3}$$

$$K_F^{(0)} = 0, \tag{A4}$$

$$\begin{aligned} K_F^{(1)} &= \frac{1}{i\omega}\sum_{n\neq 0}^{\infty}\frac{e^{-in\omega z}}{n}{}^{(n)}H \\ &= \frac{1}{i\omega}[{}^{(1)}He^{-i\omega z} - {}^{(-1)}He^{i\omega z}] \\ &= -\frac{2^{(1)}H\sin\omega z}{\omega}. \end{aligned} \tag{A5}$$

All terms except the contributions from the components H_0 and $H_{\pm 1}$ are neglected as these terms $H_l = 0$ ($|l| \geq 2$) vanish in our case. Thus, we obtain the gauge-dependent Floquet Hamiltonian in Eq. (4).

Acknowledgement

This work was supported by the National Natural Science Foundation of China (Nos. 11874266 and 11604208), the Shanghai Science and Technology Committee (Nos. 16ZR1445600 and 16ZR1445500), and the ChenGuang Program (No. 17CG49).

References

1. M. Z. Hasan and C. L. Kane, "Colloquium: topological insulators," Rev. Mod. Phys. **82**, 3045 (2010).
2. X.-L. Qi and S.-C. Zhang, "Topological insulators and superconductors," Rev. Mod. Phys. **83**, 1057 (2011).
3. T. Oka and H. Aoki, "Photovoltaic Hall effect in graphene," Phys. Rev. B **79**, 081406 (2009).
4. B. I. Halperin, "Quantized Hall conductance, current-carrying edge states, and the existence of extended states in a two-dimensional disordered potential," Phys. Rev. B **25**, 2185 (1982).
5. Q. Cheng, Y. Pan, Q. Wang, T. Li, and S. Zhu, "Topologically protected interface mode in plasmonic waveguide arrays," Laser Photonics Rev. **9**, 392 (2015).
6. T. Lin, Z. Chen, X. Zhang, H. Li, X. Liu, and H. Lü, "Experimental observation of topologically protected defect states in silicon waveguide arrays," Chin. Opt. Lett. **18**, 051301 (2020).
7. T. Kitagawa, E. Berg, M. Rudner, and E. Demler, "Topological characterization of periodically driven quantum systems," Phys. Rev. B **82**, 235114 (2010).
8. J. Cayssol, B. Dóra, F. Simon, and R. Moessner, "Floquet topological insulators," Phys. Status Solidi RRL **7**, 101 (2013).
9. M. S. Rudner and N. H. Lindner, "Band structure engineering and non-equilibrium dynamics in Floquet topological insulators," Nat. Rev. Phys. **2**, 229 (2020).
10. N. H. Lindner, G. Refael, and V. Galitski, "Floquet topological insulator in semiconductor quantum wells," Nat. Phys. **7**, 490 (2011).
11. G. Jotzu, M. Messer, R. Desbuquois, M. Lebrat, T. Uehlinger, D. Greif, and T. Esslinger, "Experimental realization of the topological Haldane model with ultracold fermions," Nature **515**, 237 (2014).
12. N. Fläschner, B. Rem, M. Tarnowski, D. Vogel, D.-S. Lühmann, K. Sengstock, and C. Weitenberg, "Experimental reconstruction of the Berry curvature in a Floquet Bloch band," Science **352**, 1091 (2016).
13. M. C. Rechtsman, J. M. Zeuner, Y. Plotnik, Y. Lumer, D. Podolsky, F. Dreisow, S. Nolte, M. Segev, and A. Szameit, "Photonic Floquet topological insulators," Nature **496**, 196 (2013).
14. B. Yang, T. Wu, and X. Zhang, "Engineering topological edge states in two dimensional magnetic photonic crystal," Appl. Phys. Lett. **110**, 021109 (2017).
15. Y. Wang, H. Steinberg, P. Jarillo-Herrero, and N. Gedik, "Observation of Floquet–Bloch states on the surface of a topological insulator," Science **342**, 453 (2013).
16. S. Sato, J. McIver, M. Nuske, P. Tang, G. Jotzu, B. Schulte, H. Hübener, U. De Giovannini, L. Mathey, and M. Sentef, "Microscopic theory for the light-induced anomalous Hall effect in graphene," Phys. Rev. B **99**, 214302 (2019).
17. A. Crespi, G. Corrielli, G. Della Valle, R. Osellame, and S. Longhi, "Dynamic band collapse in photonic graphene," New J. Phys. **15**, 013012 (2013).
18. K. Stannigel, P. Hauke, D. Marcos, M. Hafezi, S. Diehl, M. Dalmonte, and P. Zoller, "Constrained dynamics via the Zeno effect in quantum simulation: implementing non-Abelian lattice gauge theories with cold atoms," Phys. Rev. Lett. **112**, 120406 (2014).
19. A. Majumdar, A. Rundquist, M. Bajcsy, V. D. Dasika, S. R. Bank, and J. Vučković, "Design and analysis of photonic crystal coupled cavity arrays for quantum simulation," Phys. Rev. B **86**, 195312 (2012).
20. W. Tan, Y. Sun, H. Chen, and S. Q. Shen, "Photonic simulation of topological excitations in metamaterials," Sci. Rep. **4**, 3842 (2014).
21. Z. Bai, Q. Zhang, and G. Huang, "Nonlinear polaritons in metamaterials with plasmon-induced transparency," Chin. Opt. Lett. **17**, 012501 (2019).

22. T. Chen, Y. Yu, Y. Song, D. Yu, H. Ye, J. Xie, X. Shen, Y. Pan, and Q. Cheng, "Distinguishing the topological zero mode and Tamm mode in a microwave waveguide array," Ann. Phys. **531**, 1900347 (2019).
23. S. Longhi, "Self-imaging and modulational instability in an array of periodically curved waveguides," Opt. Lett. **30**, 2137 (2005).
24. I. L. Garanovich, S. Longhi, A. A. Sukhorukov, and Y. S. Kivshar, "Light propagation and localization in modulated photonic lattices and waveguides," Phys. Rep. **518**, 1 (2012).
25. M. Kremer, I. Petrides, E. Meyer, M. Heinrich, O. Zilberberg, and A. Szameit, "A square-root topological insulator with non-quantized indices realized with photonic Aharonov–Bohm cages," Nat. Commun. **11**, 907 (2020).
26. W. Song, H. Li, S. Gao, C. Chen, S. Zhu, and T. Li, "Subwavelength self-imaging in cascaded waveguide arrays," Adv. Photonics **2**, 036001 (2020).
27. G. T. Lenz, I. De Sterke, and C. Martijn, "Bloch oscillations in an array of curved optical waveguides," Phys. Rev. Lett. **83**, 963 (1999).
28. S. Weimann, M. Kremer, Y. Plotnik, Y. Lumer, S. Nolte, K. G. Makris, M. Segev, M. C. Rechtsman, and A. Szameit, "Topologically protected bound states in photonic parity–time-symmetric crystals," Nat. Mater. **16**, 433 (2017).
29. S. Longhi, M. Marangoni, M. Lobino, R. Ramponi, P. Laporta, E. Cianci, and V. Foglietti, "Observation of dynamic localization in periodically curved waveguide arrays," Phys. Rev. Lett. **96**, 243901 (2006).
30. A. Szameit, I. L. Garanovich, M. Heinrich, A. A. Sukhorukov, F. Dreisow, T. Pertsch, S. Nolte, A. Tünnermann, and Y. S. Kivshar, "Polychromatic dynamic localization in curved photonic lattices," Nat. Phys. **5**, 271 (2009).
31. O. Zilberberg, S. Huang, J. Guglielmon, M. Wang, K. P. Chen, Y. E. Kraus, and M. C. Rechtsman, "Photonic topological boundary pumping as a probe of 4D quantum Hall physics," Nature **553**, 59 (2018).
32. J. M. Zeuner, N. K. Efremidis, R. Keil, F. Dreisow, D. N. Christodoulides, A. Tunnermann, S. Nolte, and A. Szameit, "Optical analogues for massless Dirac particles and conical diffraction in one dimension," Phys. Rev. Lett. **109**, 023602 (2012).
33. J. Noh, W. A. Benalcazar, S. Huang, M. J. Collins, K. P. Chen, T. L. Hughes, and M. C. Rechtsman, "Topological protection of photonic mid-gap defect modes," Nat. Photon. **12**, 408 (2018).
34. S. Stützer, Y. Plotnik, Y. Lumer, P. Titum, N. H. Lindner, M. Segev, M. C. Rechtsman, and A. Szameit, "Photonic topological Anderson insulators," Nature **560**, 461 (2018).
35. L. J. Maczewsky, J. M. Zeuner, S. Nolte, and A. Szameit, "Observation of photonic anomalous Floquet topological insulators," Nat. Commun. **8**, 13756 (2017).
36. S. Mukherjee, A. Spracklen, M. Valiente, E. Andersson, P. Öhberg, N. Goldman, and R. R. J. N. C. Thomson, "Experimental observation of anomalous topological edge modes in a slowly driven photonic lattice," Nat. Commun. **8**, 13918 (2017).
37. B. Zhu, H. Zhong, Y. Ke, X. Qin, A. A. Sukhorukov, Y. S. Kivshar, and C. Lee, "Topological Floquet edge states in periodically curved waveguides," Phys. Rev. A **98**, 013855 (2018).
38. S. Longhi, "Light transfer control and diffraction management in circular fibre waveguide arrays," J. Phys. B **40**, 4477 (2007).
39. Q. Cheng, Y. Pan, H. Wang, C. Zhang, D. Yu, A. Gover, H. Zhang, T. Li, L. Zhou, and S. Zhu, "Observation of anomalous π modes in photonic Floquet engineering," Phys. Rev. Lett. **122**, 173901 (2019).
40. Z. Fedorova, C. Jörg, C. Dauer, F. Letscher, M. Fleischhauer, S. Eggert, S. Linden, and G. von Freymann, "Limits of topological protection under local periodic driving," Laser Photonics Rev. **8**, 63 (2019).
41. M. Mrejen, H. Suchowski, T. Hatakeyama, C. Wu, L. Feng, K. O'Brien, Y. Wang, and X. Zhang, "Adiabatic elimination-based coupling control in densely packed subwavelength waveguides," Nat. Commun. **6**, 7565 (2015).
42. M. Mrejen, H. Suchowski, T. Hatakeyama, Y. Wang, and X. Zhang, "Experimental realization of two decoupled directional couplers in a subwavelength packing by adiabatic elimination," Nano Lett. **15**, 7383 (2015).